The Astrophysical Journal, 628:931–937, 2005 August 1
© 2005. The American Astronomical Society. All rights reserved. Printed in U.S.A.

X-RAY SPECTROSCOPY OF PSR B1951+32 AND ITS PULSAR WIND NEBULA

X. H. Li,[1] F. J. Lu,[1] and T. P. Li[1,2]

Received 2004 July 29; accepted 2005 April 12

ABSTRACT

We present spatially resolved X-ray spectroscopy of PSR B1951+32 and its pulsar wind nebula (PWN) in supernova remnant (SNR) CTB 80 from a *Chandra* observation. The *Chandra* X-ray map clearly reveals various components of a ram-pressure-confined PWN embedded in the SNR ejecta: a point source representing the pulsar, X-ray emission from the bow shock, a luminous X-ray tail, a 30″ diameter plateau whose northwestern part is absent, and the more diffuse outer X-ray emission. The plateau is closely surrounded by the radio, [O III], [S II], and [N II] shells, and the outer diffuse emission is mostly within the Hα shells. While the spectra of all the features are well fitted with power-law models, a power-law plus blackbody model can fit the spectrum of the pulsar significantly better than using a power-law model alone. Generally, the spectra of these components obey the trend of steepening from the inside to the outside. However, the edge of the plateau probably has a harder spectrum than the central region of the plateau. The cause of the apparent hard spectrum of the plateau edge is unclear, but we speculate that it might be due to a shock between the PWN and the SNR ejecta. The possible blackbody radiation component from the pulsar has a temperature of 0.13 ± 0.02 keV and an equivalent emitting radius of $2.2^{+1.4}_{-0.8}$ (d/2 kpc) km, and is thus probably from the hot spots on the pulsar. We also show in this paper that the blackbody temperature of the entire surface of PSR B1951+32 is much lower than those predicted by the standard neutron star cooling models.

Subject headings: pulsars: general — stars: neutron — supernova remnants

1. INTRODUCTION

It is generally accepted that only a small fraction ($\leq$10%) of the spin-down energy of a young pulsar is converted into observable pulsed emission and that most of the energy leaves the pulsar in the form of a highly relativistic electron/positron wind. This relativistic wind eventually interacts (through a termination shock) with the external medium, emits synchrotron radiation, and produces a pulsar wind nebula (PWN; e.g., Rees & Gunn 1974; Kennel & Coroniti 1984). The pulsar wind particles are usually confined by the supernova ejecta or interstellar medium (ISM; e.g., Reynolds & Chevalier 1984), and the morphology of the PWN relies strongly on how the wind particles are confined. Some PWNe (e.g., IC 433, W44, N157B, B1957+20, B1757−24, Duck Nebula, Mouse, Geminga) have cometary morphologies, which has been attributed to the supersonic motion of their respective pulsars in the ISM or supernova remnants (SNRs; Wang et al. 1993, 2001; Olbert et al. 2001; Kaspi et al. 2001; Chatterjee & Cordes 2002; Petre et al. 2002; Caraveo et al. 2003; Lu et al. 2003; Stappers et al. 2003; Gaensler et al. 2004; Gvaramadze 2004). In such a system, a bow shock runs ahead of the pulsar, most of the wind particles are confined to the direction opposite the pulsar proper motion, and the pulsar is well offset from the center or even at the apex of the PWN (Wang et al. 1993; Wilkin 1996; Wang & Gotthelf 1998; Bucciantini 2002; Caraveo et al. 2003; van der Swaluw et al. 2003; Gaensler et al. 2004; Gvaramadze 2004; van der Swaluw 2004). Detailed spatially resolved X-ray spectroscopy of a PWN should be important for examining and refining these models, because the X-ray–emitting particles are young and have a short lifetime, and thus the spatial variations of the X-ray spectra will reflect the particle track and energy evolution in the PWN very well.

Radio and optical observations suggest that the PWN energized by PSR B1951+32 in SNR CTB 80 (G69.0+2.7) is an ideal "laboratory" in which to study the interaction between an SNR and the embedded PWN. CTB 80 has a peculiar radio morphology composed of three ridges and a $\sim$30″ core in the southern central portion of the extended component (e.g., Koo et al. 1993; Mavromatakis et al. 2001; Castelletti et al. 2003). The 39.5 ms PSR B1951+32, located at the southwestern edge of the core, moves toward the southwest ($\sim$252°, north through east) with a transverse velocity of 240 ± 40 km s^{-1} for a distance of 2 kpc (Migliazzo et al. 2002). Radio observation revealed a U-like loop and a bright bow shock feature southwest of the loop, indicating strong interaction of the wind of the fast-moving pulsar with the environment (Strom 1987; Migliazzo et al. 2002). The optical structure of the PWN of PSR B1951+32 was delineated by forbidden-line ([O III], [S II], and [N II]) emission as shell-like (Hester & Kulkarni 1988, 1989). These optical features suggest that they arise behind shocks that are being driven into a magnetized thermal plasma by the confined relativistic wind from PSR B1951+32 (Hester & Kulkarni 1989; Lozinskaya et al. 1995).

The optical and radio properties also make the PWN of PSR B1951+32 a hot target for various X-ray telescopes. The *Einstein* observations show a central filled X-ray source with a nonthermal X-ray spectrum (photon index $\alpha = 3.8^{+0.2}_{-0.3}$), and the morphology of the source has been interpreted as resulting from the relativistic jets energized by the central pulsar (Becker et al. 1982; Wang & Seward 1984). The *European X-Ray Observatory Satellite* (*EXOSAT*) observation confirmed the nonthermal nature of the X-ray spectrum but inferred a smaller photon index of 1.9 ± 0.5 (Angelini et al. 1988). Safi-Harb et al. (1995) studied CTB 80 and PSR B1951+32 with the Position Sensitive Proportional Counter (PSPC) and the High Resolution Imager (HRI)

[1] Laboratory of Particle Astrophysics, Institute of High Energy Physics, CAS, Beijing 100049, China; lixh@ihep.ac.cn, lufj@ihep.ac.cn.

[2] Department of Physics and Center for Astrophysics, Tsinghua University, Beijing, China; litp@mail.tsinghua.edu.cn.

on board *Röntgensatellit* (*ROSAT*). They found a bright compact core of $\sim 1'$ radius surrounding the pulsar and a diffuse nebula extending $\sim 5'$ eastward of the pulsar, and the spectra of these two features are both nonthermal. These observational properties are quite consistent with those of a PWN. However, due to the limited spatial and spectral resolution of the previous X-ray telescopes, the detailed morphological and spectral structures of the X-ray emission remain not well resolved.

The superb spatial resolution and moderately good spectral resolution of the *Chandra X-Ray Observatory* permit a detailed morphological study and spatially resolved X-ray spectroscopy of PSR B1951+32 and its PWN. *Chandra* can isolate the pulsar from the surrounding nebula, and we can then study the spectrum of the pulsar proper, which has not yet been done. The lifetime of the synchrotron X-ray–emitting particles is short, and therefore the spectral variation across the nebula presents important clues to the particle acceleration and the energy-losing processes. Recently, Moon et al. (2004) studied the high-resolution X-ray (with *Chandra*), Hα (with the *Hubble Space Telescope* [*HST*]), and IR (with the 5 m Palomar Hale telescope) structures of the region around PSR B1951+32 and identified a cometary PWN that appears to be confined by a bow shock produced by the high-velocity motion of the pulsar. In this paper, we give more detailed analyses of the *Chandra* data. We introduce the data reduction in § 2, present our analyses and results in § 3, discuss the structure of the PWN in § 4, and conclude our work in § 5. Throughout the paper, the errors are at the 90% significance level.

2. OBSERVATION AND DATA REDUCTION

Chandra observed the PWN of PSR B1951+32 with the Advanced CCD Imaging Spectrometer (ACIS) on 2001 July 19 with an exposure time of 74 ks. The target was positioned at the aim point on the back-illuminated ACIS-S3 in VFAINT mode and at a working temperature of -120° C. ACIS is sensitive to X-rays in 0.2–10 keV with an energy resolution of $\Delta E/E \sim 0.1$ at 1 keV, and the FWHM of the point-spread function (PSF) is $0\farcs5$. The frame readout time for this observation is 0.74 s, since only a small portion of the CCD chip was illuminated.

We calibrated the data using CIAO (ver. 3.1) and CALDB (ver. 2.27). We reprocessed the Level 1 data for correction of the charge transfer inefficiency (CTI) effects, cleaned the background, and removed the afterglow. Time intervals with anomalous background rates associated with particle flare events were further rejected for the Level 2 data, and the final net exposure time was 71 ks. The spectra were fitted with XSPEC.

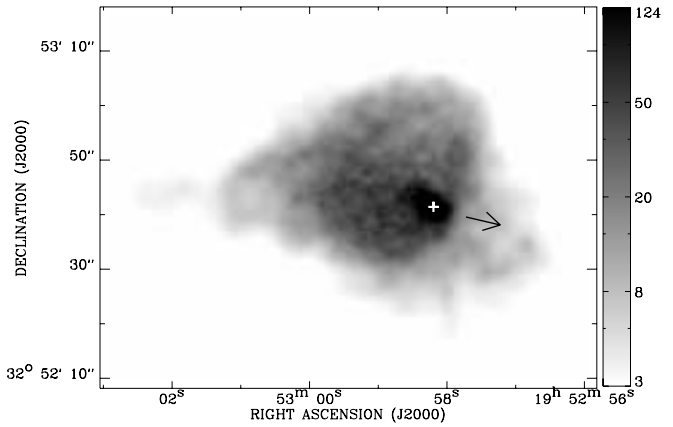


FIG. 1.—*Chandra* ACIS image of the PWN of PSR B1951+32, adaptively smoothed with a Gaussian filter to achieve a signal-to-noise ratio ≥ 12. The plus sign indicates the position of PSR B1951+32, and the arrow indicates the direction of the pulsar proper motion. The gray scale increases logarithmically from 3.3 to 124 counts per square arcsecond after smoothing.

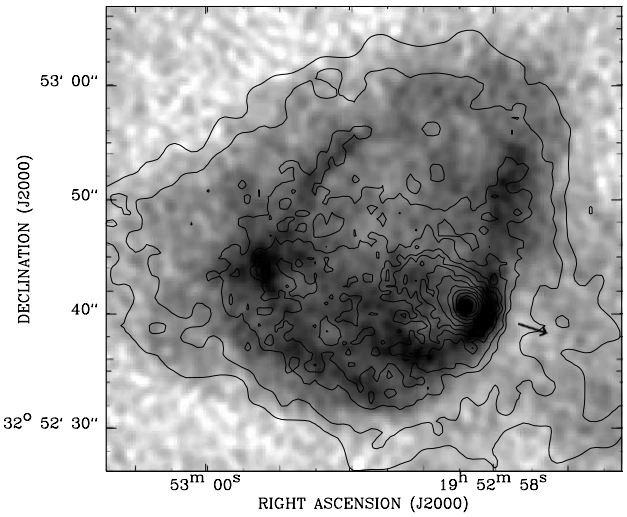


FIG. 2.—The 0.3–8.0 keV X-ray contours (levels: 12, 29, 41, 62, 83, 124, 206, 413, 826, 1652, and 3304 counts per square arcsecond after smoothing) of the PWN of PSR B1951+32 superposed on the 20 cm radio image from Migliazzo et al. (2002). The arrow indicates the direction of pulsar proper motion.

3. ANALYSIS AND RESULTS

3.1. *Spatial Structure*

Figure 1 shows an ACIS image of the PWN of PSR B1951+32. This image reveals several major components of the PWN: a point source at R.A. (J2000) = $19^{\rm h}52^{\rm m}58\fs20$, decl. (J2000) = $32^\circ 52' 40\farcs7$; a bright elongation northeast of the point source; a $30''$ diameter plateau with absence in its northwest section; and more diffuse emission in between and beyond these features. The position of the point source was obtained by the `celldetect` tool in CIAO and has an uncertainty $\sim 0\farcs2$, which is quite consistent with the radio position of PSR B1951+32 (Migliazzo et al. 2002). The X-ray point source thus represents the X-ray emission from this pulsar. The X-ray plateau is just within the radio and optical shells (Hester & Kulkarni 1989) and therefore corresponds to the main body of the PWN. The overall structure of the X-ray nebula is similar to the radio structure, as shown in Figure 2, except that the radio nebula is limb brightened and that the bright X-ray elongation in the northeast is absent in the radio map (Strom 1987; Migliazzo et al. 2002).

In order to show the diffuse X-ray emission near the pulsar more clearly, we plot in Figure 3 the X-ray count (per $0\farcs492 \times 0\farcs492$ pixel) profile (*solid line*) along the pulsar proper motion. In this profile the contribution from the pulsar has been removed by subtracting the convolution of a delta function with the telescope PSF. The PSF is energy weighted and was simulated with ChaRT.[3] The dashed line in Figure 3 represents the 1.5 GHz radio profile from Migliazzo et al. (2002). It is clear that there is high brightness diffuse emission within $\sim 2''$ radii from the pulsar. There is also significant X-ray emission in the radio bow shock region, although the overall trend of the diffuse emission is declining.

3.2. *Spectra*

According to our analyses of the morphology of the nebula, we divided it into a few regions (see Fig. 4), from which we

[3] See http://cxc.harvard.edu/chart/threads/index.html.

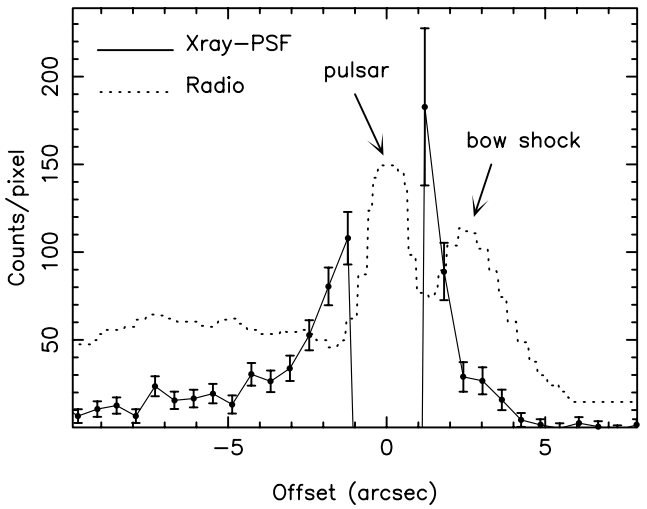


FIG. 3.—The 0.3–8.0 keV X-ray intensity profile (*solid line*; with the pulsar contribution subtracted, pixel size is $0''.492 \times 0''.492$) and the radio profile (*dotted line*) along the proper motion direction of PSR B1951+32. The radio data are taken from Fig. 2 of Migliazzo et al. (2002) and plotted on an arbitrary linear scale. The *x*-axis represents the offset from the pulsar.

extracted the spectra of various components. The background used in the spectral analysis of the diffuse features was extracted from two boxes in which there was no prominent emission, while the background of the pulsar spectrum was extracted from an annulus centered on the pulsar, with inner and outer radii of $1''.5$ and $3''$, respectively. We fitted the spectra of the diffuse features jointly with a power-law (PL) model by forcing all the spectra to share the same absorbing column density ($N_{\rm H}$). As shown in Figure 5, such a model fits the spectra very well. The resulting $N_{\rm H}$ is $3.0 \pm 0.1 \times 10^{21}$ cm^{-2}, and the other parameters are listed in Table 1. As seen in other PWNe, these spectra display a trend of softening with distance from the pulsar due to the fast energy loss of the high-energy electrons (e.g., Slane et al. 2002; Lu et al. 2002; Kaspi et al. 2005).

The pile-up fraction of the pulsar emission was estimated as 6% using Sherpa, and thus the pile-up effect was neglected in our analysis of the pulsar spectrum. We first fitted the pulsar spectrum with a PL model by fixing the column density at 3.0×10^{21} cm^{-2}, as derived above. This gives a photon index of 1.74 ± 0.03 and χ^2 of 223 with 208 degrees of freedom (dof). We then fitted the spectrum with a power-law plus blackbody (PL+BB) model, and this yields a photon index of $1.63^{+0.03}_{-0.05}$, BB temperature

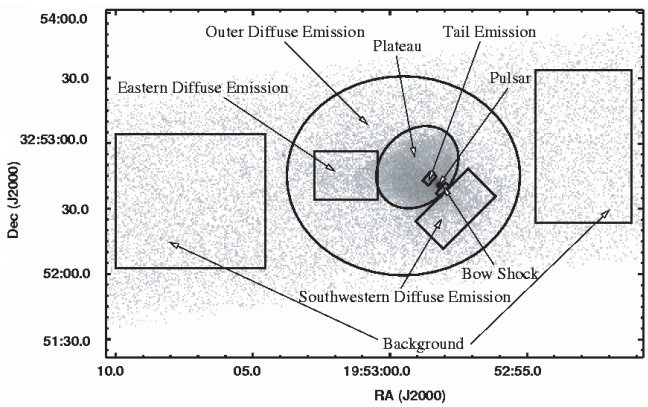


FIG. 4.—*Chandra* ACIS image of the PWN of PSR B1951+32. The regions show where the spectra are extracted, and the fitted parameters are listed in Table 1.

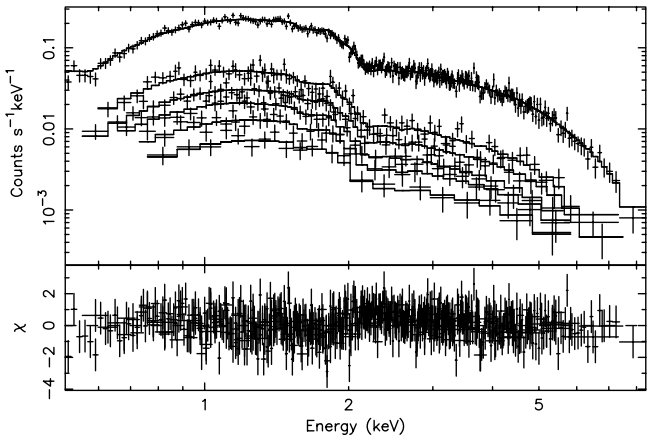


FIG. 5.—Power-law model fits to the spectra of different regions defined in Fig. 4. From top to bottom, the spectra are of the plateau, outer diffuse emission, southwest diffuse emission, east diffuse emission, tail emission, and bow shock regions.

of 0.13 ± 0.02 keV, and a χ^2 of 190 with 206 dof. If we only check the data in 0.5–1.5 keV (the energy region to which the BB component contributes), the χ^2 and dof of the spectral fitting with and without the BB component are 61 and 60, and 84 and 62, respectively. The `ftest` task shows that the substitution of the PL model by the PL+BB model is necessary at a significance level of >99.99%. In comparison, Figure 6 gives the 0.5–1.5 keV spectrum of the pulsar fitted with a PL model and a PL+BB model. The fitted BB flux corresponds to an equivalent emitting radius of $2.2^{+1.4}_{-0.8}$ km assuming a distance of 2.0 kpc to the pulsar.

In order to see whether there is any spectral variation in the plateau or in the very outer region surrounding the plateau, we extracted spectra from the five quasi-annulus regions defined in Figure 7 and fitted them with a PL model using a background identical to that used above. Table 2 lists the spectral fitting results, which show that the edge of the plateau (rings 1, 2, and 3 in Table 2, and thus the radio shell region) apparently has a harder

TABLE 1

THE SPECTRAL FITTING PARAMETERS OF PSR B1951+32 AND ITS PWN

Region (1)	Γ/T (keV) (2)	Flux (3)
Point source		
Power-law plus blackbody:		
Power-law	1.63 ± 0.05	35 ± 3
Blackbody	0.13 ± 0.02	3^{+14}_{-3}
Power-law	1.74 ± 0.03	35 ± 2
Bow shock	$1.6^{+0.1}_{-0.2}$	$2.1^{+0.9}_{-0.4}$
Tail emission	1.6 ± 0.1	3.6 ± 0.7
Plateau	1.69 ± 0.04	61 ± 4
Southwestern diffuse emission	$1.77^{+0.09}_{-0.07}$	8.0 ± 0.9
Eastern diffuse emission	1.8 ± 0.1	5.4 ± 0.7
Outer diffuse emission	$1.88^{+0.08}_{-0.07}$	13 ± 1
Entire nebula	1.73 ± 0.03	96 ± 5

NOTE.—The X-ray absorbing column density $N_{\rm H}$ is obtained by jointly fitting the spectra of various diffuse components as $(3.0 \pm 0.1) \times 10^{21}$ cm^{-2}. We rebinned the spectra before fitting so that data in each rebinned channel have signal-to-noise ratio ≥ 6. The overall χ^2 is 401 for 544 dof for the diffuse components. The unabsorbed flux density (10^{-13} ergs cm^{-2} s^{-1}) in 0.2–10 keV is listed in col. (3).

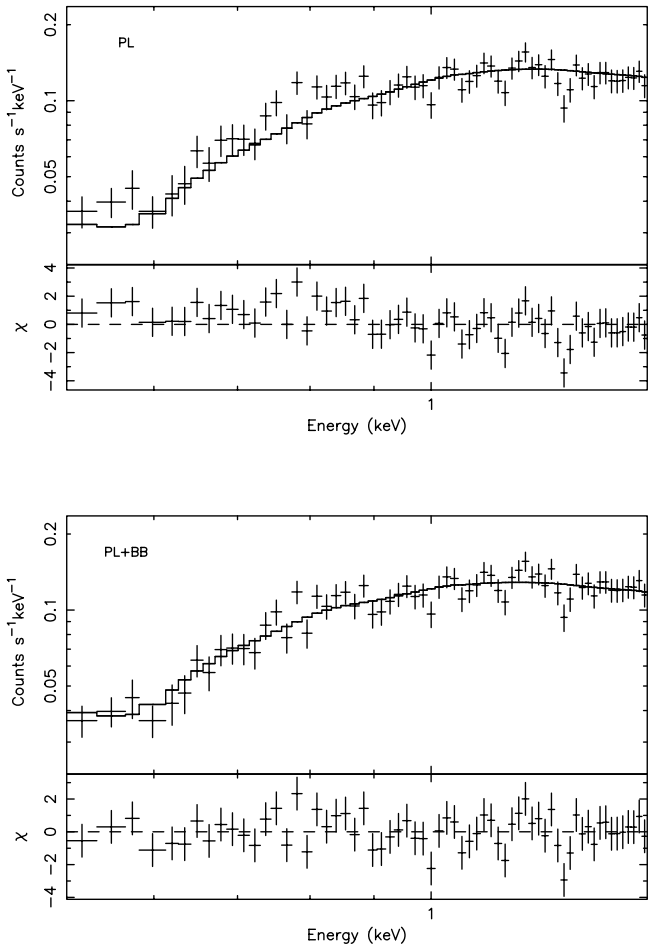


FIG. 6.—Spectral fitting to PSR B1951+32. The figures show only data in 0.5–1.5 keV. The top panel shows the fit with a PL model, and the bottom panel shows the fit with a PL+BB model.

spectrum than that of the neighboring inner (the center region) and outer regions (ring 4).

A Monte Carlo simulation has been used to estimate how much flatter the spectrum of the plateau edge is than that of the center region. We generated 100,000 pairs of random numbers. In each pair, the first is a random number from a Gaussian distribution with mean and standard deviation of 1.76 and 0.04, respectively, while the second number is from a Gaussian distribution with mean and standard deviation of 1.64 and 0.015, respectively. The standard deviations are smaller than the error listed in Table 2, since those in Table 2 are at a 90% significance level. We found that only 235 out of the 100,000 pairs have first numbers that are smaller than the corresponding second numbers. Therefore, the overall spectrum of rings 1 to 3 is flatter than the spectrum of the center region at a significance of 99.7%.

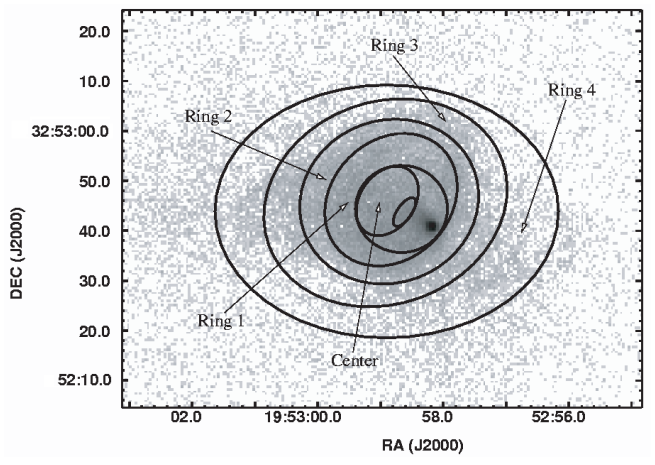


FIG. 7.—*Chandra* ACIS image of the PWN of PSR B1951+32. The quasi-annuli in this figure define regions from which the spectra listed in Table 2 are extracted.

TABLE 2
THE SPECTRAL FITTING RESULTS OF THE FIVE QUASI-ANNULUS REGIONS

	$N_H = 3.0 \times 10^{21}$ cm^{-2}		$\Gamma = 1.70 \pm 0.05$
REGIONS (1)	Γ (2)	Flux (3)	N_H (10^{21} cm^{-2}) (4)
Center	1.76 ± 0.06	10 ± 1	2.8 ± 0.2
Ring 1	1.66 ± 0.04	20 ± 1	3.2 ± 0.2
Ring 2	1.65 ± 0.05	14 ± 1	3.2 ± 0.2
Ring 3	1.66 ± 0.10	10 ± 1	3.1 ± 0.2
Ring 4	1.81 ± 0.08	8 ± 1	2.6 ± 0.3
Ring 123	1.64 ± 0.02	42 ± 2	3.3 ± 0.2

NOTE.—Cols. (2) and (3) are fitted photon indices (Γ) and unabsorbed fluxes (10^{-13} ergs cm^{-2} s^{-1}) in 0.2–10 keV, respectively; when N_H is fixed as 3.0×10^{21} cm^{-2}, the χ^2 is 350 for 530 dof. Col. (4) gives fitted N_H (10^{21} cm^{-2}) and unabsorbed fluxes (10^{-13} ergs cm^{-2} s^{-1}) by forcing all spectra (except ring 123) to share the same Γ (which was derived as 1.70 ± 0.05), and the corresponding χ^2 is 348 for 529 dof. The spectrum index of ring 123 is obtained with $N_H = 3.0 \times 10^{21}$ cm^{-2}, and the χ^2 is 204 for 241 dof. The N_H of ring 123 is obtained with $\Gamma = 1.70$, and the χ^2 is 196 for 241 dof.

We have also fitted the spectrum of the entire nebula (excluding the pulsar) with a PL model. This gives an N_H of $3.0 \pm 0.1 \times 10^{21}$ cm^{-2}, a photon index of 1.73 ± 0.03, an unabsorbed 0.2–10 keV energy flux of 9.6×10^{-12} ergs cm^{-2} s^{-1}, and χ^2 of 296 for 312 dof.

4. DISCUSSION

4.1. *The Magnetic Field Strength in the Nebula*

The radio and X-ray spectra of the PWN can be used to estimate the magnetic field strength in the nebula. The radio emission of this PWN has a flat spectrum of $\alpha = 0$ ($F_\nu \sim \nu^{-\alpha}$) and flux of $\sim$500 mJy (Angerhofer et al. 1981). In § 3.2 we infer that these two values for the X-ray emission are 0.73 and 1 μJy, respectively. Therefore the spectral break frequency ν_{br} between the radio and X-ray band is around 10^{10} Hz. Assuming that this spectral break arises from synchrotron losses, the magnetic field in the nebula is then determined by the age of this nebula. The proper motion of the pulsar indicates that the pulsar can cross the X-ray plateau in about 1200 yr. Nonetheless, this seems unlikely to be the age of the PWN of PSR B1951+32. Most of the electrons injected by the pulsar are probably still confined in the bubble by the highly ordered magnetic field (Hester & Kulkarni 1988), as indicated by the much higher radio brightness of this region (compared to that of the neighboring regions) and the nice radio shells (Migliazzo et al. 2002). Therefore, we use the pulsar dynamic age (64 kyr; Migliazzo et al. 2002) to represent the age of the PWN. Using the formula reproduced by Frail et al. (1996) from Pacholczyk (1970), we found that the magnetic field strength in the nebula is $\sim$300 μG. This estimated magnetic field strength is comparable to the values given by Angerhofer et al. (1981), Hester & Kulkarni (1989), and Moon et al. (2004), but much

higher than those given by Safi-Harb et al. (1995) and Castelletti et al. (2003).

The discrepancy between our result and that (5.2 μG) of Castelletti et al. (2003) is due to the fact that they used a much higher $\nu_{\rm br}$ of 2.4×10^{16} Hz and a much lower PWN age of 18,200 yr. We found that both the high $\nu_{\rm br}$ and the low PWN age are problematic. Their reason for choosing $\nu_{\rm br} = 2.4 \times 10^{16}$ Hz is that $\nu_{\rm br}$ is not much lower than the X-ray energies given the similar X-ray and radio sizes of the PWN. However, as we discuss above, the PWN has similar X-ray and radio sizes most likely because the pulsar wind particles are well confined rather than diffused freely. The time for the pulsar to move across the $\sim 10'$ radio nebula is 18,200 yr. But again, most of the wind particles ejected by the pulsar are likely still in the bubble. To use the pulsar dynamic age as the PWN age is more reasonable.

We now discuss whether the spectral break between the radio and X-ray bands is mainly due to synchrotron cooling. Kaspi et al. (2001) suggested that more than one electron population is being injected into the PWN of PSR B1757−24. The injected wind particles of PSR B1951+32 may have similar energy spectra. However, synchrotron cooling does play an important role in the X-ray to radio spectrum in the PWN of PSR B1951+32. The particle energy spectrum of the bright X-ray tail (see Figs. 1 and 3) may represent the injected particle energy spectrum well, because these particles are young. The nondetection of radio emission in this region suggests that the current overall particle energy spectrum in the PWN is significantly steeper than the injected one, due to synchrotron cooling. Therefore, although not very certain, the magnetic field strength we obtained is reasonable.

4.2. *The PWN Geometry*

The PWN of PSR B1951+32 represents the pulsar wind material confined by the ram pressure of the ambient medium, a typical example of the model suggested by many authors (e.g., Wilkin 1996; Wang & Gotthelf 1998; Bucciantini 2002; van der Swaluw et al. 2003; Gaensler et al. 2004; van der Swaluw 2004). It has the following regions:

The pulsar wind cavity and termination shock.—In the immediate region surrounding the pulsar the relativistic wind flows freely outward with very little emission, and this region is shown as a cavity. The size of the cavity is determined by the radius of the termination shock over which the pulsar wind ram pressure ($\dot{E}/4\pi r^2 c$) balances the ram pressure of the ISM due to the motion of the pulsar ($\rho_a v_{\rm psr}^2$), where ρ_a is the ambient medium density, $v_{\rm psr}$ and $\dot{E}$ are the velocity and spin-down energy of the pulsar, r is the radius of the termination shock, and c is the speed of light. For PSR B1951+32, $\rho_a \sim 50 \times 1.67 \times 10^{-24}$ g cm^{-3} $= 8.4 \times 10^{-24}$ g cm^{-3} (Hester & Kulkarni 1989), $v_{\rm psr} \sim 240$ km s^{-1}, $\dot{E} = 3.7 \times 10^{36}$ ergs s^{-1}, and thus $r \sim 1.4 \times 10^{16}$ cm, corresponding to $0\farcs5$ at the distance (2.0 kpc) to the pulsar. Because PSR B1951+32 moves supersonically in the SNR, as the simulation shows (e.g., Gaensler et al. 2004), this region is more likely elongated opposite to the pulsar proper motion rather than elongated spherically.

In the X-ray count profile of the nebula along the pulsar proper motion (Fig. 3), we see strong diffuse emission in the nearby region of the pulsar. The FWHM of this emission is about $3''$, and the emission following the pulsar extends a little farther out ($\sim 3''$ compared to $\sim 2''$) than that ahead of the pulsar. We propose that this high brightness region most likely represents the emission from the termination shock, giving its roughly similar angular sizes. The bigger extension opposite to the pulsar proper motion is consistent with the distorted termination shock geometry because of the supersonic motion of the pulsar (Gaensler et al. 2004). The pulsar wind cavity in this nebula is unresolved, giving the contamination from the high brightness emission from the pulsar and the termination shock.

The particle tunnel.—The X-ray elongation (tail) about $4''$ to $10''$ northeast of the pulsar most likely represents the particle tunnel suggested by Wang & Gotthelf (1998) and Gaensler et al. (2004; see region B2 in their Fig. 9). Reasons to identify this emission as from the particle tunnel rather than from the termination shock are the tail-like morphology and its much lower brightness than that of the region neighboring the pulsar. The bright radio and X-ray features at R.A. $= 19^{\rm h}52^{\rm m}59\fs6$, decl. $= 32^\circ 52' 44''$ (J2000) (Fig. 2; Strom 1987; Migliazzo et al. 2002) may represent the termination site of the particle tunnel (Wang & Gotthelf 1998). Since this bright radio feature does not align with the pulsar's motion, it is possible that the particle tunnel has been bent due to interaction with a gradient in the ambient density and/or magnetic field, as also seen in the Crab Nebula and the PWN of PSR B1509−58 (Weisskopf et al. 2000; Gaensler et al. 2002).

The interface between the PWN and SNR.—In § 3.1 we mention that the bright X-ray plateau is well surrounded by the radio and [O III], [S II], and [N II] shells. This implies that the main body of the PWN is well confined by the SNR ejecta. The radio map is much more shell-like than the X-ray map, suggesting that the old wind particles have accumulated at the interface between the PWN and SNR, since the radio-emitting particles have a much longer lifetime than the X-ray–emitting particles. As suggested by Hester & Kulkarni (1988), there may exist a highly ordered magnetic field in the shell, which might prevent the old particles from diffusing out.

The low surface brightness X-ray diffuse emissions in front of the bow shock and outside the eastern edge of the PWN are positionally consistent with the bipolar Hα structure (Fig. 2 of Moon et al. 2004). We propose that this is the consequence of the nonuniform distribution of the SNR ejecta. In the directions of the two low surface brightness X-ray protrusions, the ejecta are of such low density that they cannot effectively confine the wind particles, so the wind particles extend farther out. Finally, the wind particles are stopped by the ISM that has low metallicity, and the interaction between them ionizes the hydrogen in the ISM to be Hα emitting.

4.3. *The Origin of the Apparent Hard Edge of the X-Ray Plateau*

Here we discuss the origin of the possible spectral hardening at the plateau edge. Although generally the apparent harder spectrum can be the result of either a higher $N_{\rm H}$ or an intrinsic hardening of the emitting spectrum, the first possibility can be ruled out for the hard edge of the X-ray plateau in this PWN. As shown in Table 2, with the photon index (Γ) fixed, $N_{\rm H}$ to the plateau edge needs to be $4 \pm 3 \times 10^{20}$ cm^{-2} higher than that to the neighboring regions. From the radio and optical observations, we know that the shell has a width of ~ 0.03 pc and an inner radius of about 0.1 pc. If the higher $N_{\rm H}$ to the plateau edge (and thus the radio shell) is due to the additional absorbing material in the shell, the required number density of the shell will be $\sim (1600 \pm 1200)$ cm^{-3}, about 20 times higher than 50–100 cm^{-3}, the value measured in optical observations (Hester & Kulkarni 1989). This implies that the apparent X-ray spectrum hardening of the edge of the plateau is not a consequence of the higher absorption but rather an intrinsically harder emitting spectrum.

In turn, the intrinsically harder emitting spectrum may be due to either the reacceleration of the pulsar wind particles at the edge or a contribution from a second emission component there. For both cases, a shock wave is needed, and a shock wave at the interface between the PWN and SNR ejecta has already been proposed by Hester & Kulkarni (1989) to explain the filamentary optical emission from the core of CTB 80. This shock is in the SNR ejecta rather than in the PWN because of the high sound velocity ($c/3^{1/2}$) in the PWN, and thus the shock cannot reaccelerate the pulsar wind particles. However, it is possible that this shock accelerates new relativistic particles, and these particles radiate synchrotron X-ray emission at the shock front, such as those observed from several SNRs (e.g., Koyama et al. 1995). This shock-generalized X-ray emission might have a flat spectrum, which makes the overall spectrum of the X-ray emission from this region harder than those from neighboring regions.

4.4. *Constraints on the Neutron Star Cooling Models*

The cooling of the neutron star (NS; age $<10^5$ yr) is realized mainly by neutrino emission from the entire stellar body. The standard cooling model only includes neutrino emission via the modified Urca process, and the nonstandard models involve pion (kaon) condensates, strong magnetic fields, or neutron superfluidity (e.g., Page 1998; Slane et al. 2002; Yakovlev et al. 2002; Yakovlev & Pethick 2004).

With the *Chandra* observation, we estimated the effective blackbody temperature of the entire surface of PSR B1951+32 and compared it with the cooling models. The majority of equations of state yield an effective NS radius larger than 12 km for any range of masses (Haensel 2001). In order to estimate the blackbody temperature of PSR B1951+32, we fitted its X-ray spectrum with a PL+BB model by fixing the emitting radius as 12 km and obtained a blackbody temperature of 7.4×10^5 K with a 3 σ upper limit of 7.8×10^5 K. In Figures 8 and 9 we plot this temperature upper limit and the various theoretical NS surface cooling curves. In these figures the pulsar's dynamic age (64 ± 18 kyr) has been used, but the characteristic age of 107 kyr is not much larger than the dynamic age (Migliazzo et al. 2002; Fruchter et al. 1988) and will not change the results much. Similar to Slane et al. (2002) and Halpern et al. (2004), the effective blackbody temperature falls considerably below the predictions of the standard cooling models, suggesting the presence of some exotic cooling contribution (such as pion/kaon condensates or strong magnetic field effects) in the interior (Slane et al. 2002; Yakovlev et al. 2002). The influence of the mass on the cooling of the NS has been discussed by Yakovlev et al. (2002). The larger mass NS tends to cool faster because the modified or direct Urca processes are less suppressed by strong proton superfluidity. As seen in Figure 9, our result may also indicate that the mass of PSR B1951+32 is higher than 1.42 $M_\odot$.

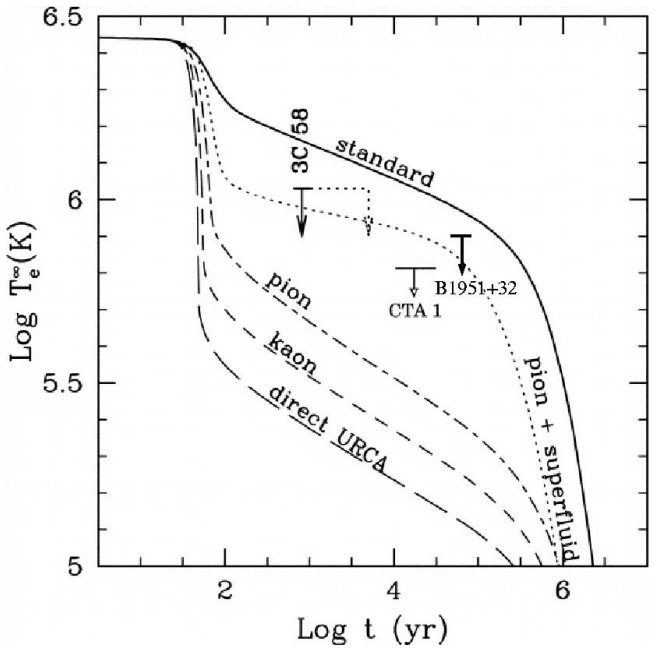


FIG. 8.—Cooling models of a 1.4 $M_\odot$ neutron star (Page 1998). PSR B1951+32 is plotted with the dark filled arrow. This figure is reproduced from Slane et al. (2002) and Halpern et al. (2004) with their permission.

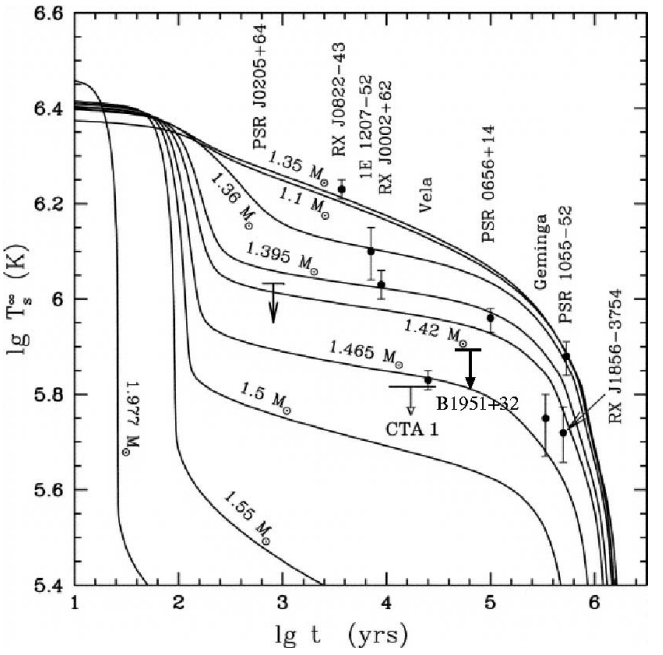


FIG. 9.—Cooling models calculated assuming strong proton superfluidity and weak neutron superfluidity (Yakovlev et al. 2002). PSR B1951+32 is plotted with the dark filled arrow. This figure is reproduced from Yakovlev et al. (2002) and Halpern et al. (2004) with their permission.

In § 3.2 we point out that there is a 0.13 keV blackbody component in the X-ray spectrum of PSR B1951+32. However, this component is not from the entire NS surface giving the small equivalent emitting radius. In the preceding paragraph, this component was not excluded in deriving the temperature of the entire surface of PSR B1951+32, and thus this surface temperature upper limit is modest. If the emission from the surface of a NS is not a blackbody, then the modification by the presence of an atmospheric component other than H will not make the temperature of the NS surface higher than the estimated effective temperature upper limit (Slane et al. 2002). In short, the above upper limit of the surface temperature of PSR B1951+32 and its constraints on the NS cooling models are safe.

5. CONCLUSIONS

We studied the morphology and spectra of PSR B1951+32 and its PWN. The overall morphology of the PWN is very consistent with a ram-pressure-confined PWN. The X-ray map shows a bright plateau that is within the radio and optical shells positionally and thus represents the main body of a PWN confined in

the SNR. We find that the spectrum of the edge of the X-ray plateau is probably harder than those of the neighboring regions, which are possibly due to the shock between the PWN and the SN ejecta. We detected thermal X-ray emission from hot spots on the NS, and the temperature of the entire surface of PSR B1951+32 is shown to be much lower than that predicted by the standard NS cooling model.

We thank the anonymous referee for his/her invaluable comments and suggestions, which led to significant improvement of the paper. We also thank Professors Mei Wu and Yong Chen of IHEP, and Professor Yang Chen of Nanjing University for discussions and suggestions. This work is supported by the Special Funds for Major State Basic Research Projects and the National Natural Science Foundation of China.

REFERENCES

Angelini, L., White, N. E., Parmar, A. N., Smith, A., & Stevens, M. A. 1988, ApJ, 330, L43
Angerhofer, P. E., Strom, R. G., Velusamy, T., & Kundu, M. R. 1981, A&A, 94, 313
Becker, R. H., Helfand, D. J., & Szymkowiak, A. E. 1982, ApJ, 255, 557
Bucciantini, N. 2002, A&A, 387, 1066
Caraveo, P. A., Bignami, G. F., DeLuca, A., Mereghetti, S., Pellizzoni, A., Mignani, R., Tur, A., & Becker, W. 2003, Science, 301, 1345
Castelletti, G., Dubner, G., Golap, K., Goss, W. M., Velázquez, P. F., Holdaway, M., & Rao, A. P. 2003, AJ, 126, 2114
Chatterjee, S., & Cordes, J. M. 2002, ApJ, 575, 407
Frail, D. A., Giacani, E. B., Goss, W. M., & Dubner, G. 1996, ApJ, 464, L165
Fruchter, A. S., Taylor, J. H., Backer, D. C., Clifton, T. R., & Foster, R. S. 1988, Nature, 331, 53
Gaensler, B. M., Arons, J., Kaspi, V. M., Pivovaroff, M. J., Kawai, N., & Tamura, K. 2002, ApJ, 569, 878
Gaensler, B. M., van der Swaluw, E., Camilo, F., Kaspi, V. M., Baganoff, F. K., Yusef-Zadeh, F., & Manchester, R. N. 2004, ApJ, 616, 383
Gvaramadze, V. V. 2004, A&A, 415, 1073
Haensel, P. 2001, A&A, 380, 186
Halpern, J. P., Gotthelf, E. V., Camilo, F., Helfand, D. J., & Ransom, S. M. 2004, ApJ, 612, 398
Hester, J. J., & Kulkarni, S. R. 1988, ApJ, 331, L121
———. 1989, ApJ, 340, 362
Kaspi, V. M., Gotthelf, E. V., Gaensler, B. M., & Lyutikov, M. 2001, ApJ, 562, L163
Kaspi, V. M., Roberts, M. S. E., & Harding, A. K. 2005, in Compact Stellar X-Ray Sources, ed. W. H. G. Lewin & M. van der Klis (Cambridge: Cambridge Univ. Press), in press (astro-ph/0402136)
Kennel, C. F., & Coroniti, F. V. 1984, ApJ, 283, 694
Koo, B., Yun, M., Ho, P. T. P., & Lee, Y. 1993, ApJ, 417, 196
Koyama, K., Petre, R., Gotthelf, E. V., Hwang, U., Matsuura, M., Ozaki, M., & Holt, S. S. 1995, Nature, 378, 255
Lozinskaya, T. A., Komarova, V. N., Moiseev, A. V., & Blinnikov, S. I. 2005, Astron. Lett., 31, 245
Lu, F. J., Wang, Q. D., Aschenbach, B., Durouchoux, P., & Song, L. M. 2002, ApJ, 568, L49
Lu, F. J., Wang, Q. D., & Lang, C. C. 2003, AJ, 126, 319
Mavromatakis, F., Ventura, J., Paleologou, E. V., & Papamastorakis, J. 2001, A&A, 371, 300
Migliazzo, J. M., Gaensler, B. M., Backer, D. C., Stappers, B. W., van der Swaluw, E., & Strom, R. G. 2002, ApJ, 567, L141
Moon, D.-S., et al. 2004, ApJ, 610, L33
Olbert, C. M., Clearfield, C. R., Williams, N. E., Keohane, J. W., & Frail, D. A. 2001, ApJ, 554, L205
Pacholczyk, A. G. 1970, Radio Astrophysics (San Francisco: Freeman)
Page, D. 1998, in The Many Faces of Neutron Stars, ed. R. Buccheri, J. van Paradijs, & M. A. Alpar (Dordrecht: Kluwer), 539
Petre, R., Kuntz, K. D., & Shelton, R. L. 2002, ApJ, 579, 404
Rees, M. J., & Gunn, J. E. 1974, MNRAS, 167, 1
Reynolds, S. P., & Chevalier, R. A. 1984, ApJ, 278, 630
Safi-Harb, S., Ogelman, H., & Finley, J. P. 1995, ApJ, 439, 722
Slane, P. O., Helfand, D. J., & Murray, S. S. 2002, ApJ, 571, L45
Stappers, B. W., Gaensler, B. M., Kaspi, V. M., van der Klis, M., & Lewin, W. H. G. 2003, Science, 299, 1372
Strom, R. G. 1987, ApJ, 319, L103
van der Swaluw, E. 2004, Adv. Space Res., 33, 475
van der Swaluw, E., Achterberg, A., Gallant, Y. A., Downes, T. P., & Keppens, R. 2003, A&A, 397, 913
Wang, Q. D., & Gotthelf, E. V. 1998, ApJ, 494, 623
Wang, Q. D., Gotthelf, E. V., Chu, Y.-H., & Dickel, J. R. 2001, ApJ, 559, 275
Wang, Q. D., Li, Z., & Begelman, M. C. 1993, Nature, 364, 127
Wang, Z. R., & Seward, F. D. 1984, ApJ, 285, 607
Weisskopf, M. C., et al. 2000, ApJ, 536, L81
Wilkin, F. P. 1996, ApJ, 459, L31
Yakovlev, D. G., Kaminker, A. D., Haensel, P., & Gnedin, O. Y. 2002, A&A, 389, L24
Yakovlev, D. G., & Pethick, C. J. 2004, ARA&A, 42, 169